Development of a microfluidic device for a future brain-organoid computing device.

Maxx Yung[1*], Sam Azadi[2†], Isabella Huang[3‡]

1 Department of Materials Science and Engineering, University of Pennsylvania
2 Singh Center for Nanotechnology, University of Pennsylvania
3 Department of Electrical and Systems Engineering, University of Pennsylvania

* myung11@seas.upenn.edu
†azadi@seas.upenn.edu
‡ ihuangg@seas.upenn.edu

Abstract

This report presents the design, simulation, and fabrication of a microfluidic platform optimized for neuromorphic computing applications using living neural networks. The design features hexagonal wells ($34.64\,\mu$m side length) connected by $20\,\mu$m channels in a honeycomb pattern. Computational fluid dynamics analysis implemented a mesh structure of $988,203$ cells and 3.8 million nodes, achieving high mesh quality metrics (0.934 orthogonal quality, 0.008 skewness) with strong convergence. At flow rates of 0.1–$1\,\mu$L/min, pressure analysis revealed drops from $850\,$Pa to $0\,$Pa (average) and $1.58\,$kPa peak pressures across the simulated segment. Extrapolated to the full $50,000\,\mu$m device length, this indicates pressure differentials of $177\,$kPa (average) and $329\,$kPa (maximum). Photolithographic fabrication successfully produced the designed patterns, though with some edge roughness and corner rounding at feature interfaces. Future work will involve experimental flow characterization to validate computational predictions and optimize device performance.

Introduction

The rapid growth in artificial intelligence computational demands has exposed fundamental limitations in traditional computing technologies [1]. As Moore's law approaches its physical limits, computing systems face increasing energy efficiency challenges [2], prompting companies to explore extreme solutions like nuclear-powered data centers. Digital computing architectures struggle to match the remarkable energy efficiency observed in biological neural networks, which achieve complex computations through probablistic and memory efficient computation [3].

Biological computing using living neuronal networks presents a promising alternative to conventional computational approaches [4–7]. However, the success of such systems critically depends on maintaining precise cellular environments. Critical parameters include maintaining pH at 7.2-7.4 through continuous CO_2 buffering, temperature stability at 37 ± 0.5°C, and more importantly, regular media exchange every $48 - 72$ hours to replenish glucose nutrient media while removing metabolic waste products [7, 8]. Manual media exchange, typically performed every 1–3 days, causes erratic nutrient fluctuations, toxic buildup, and exposure to suboptimal conditions during media replenishment. Automated microfluidic systems address these issues by maintaining

precise, continuous nutrient delivery and waste removal, minimizing cellular stress and replicating physiological conditions more accurately [8].

This undergraduate research project aims to simulate and develop a microfluidic platform optimized for future neuromorphic applications. The focus will be on understanding computational fluid dynamics, lithography techniques, and designing a microfluidic system to achieve precise flow control ($0.1 - 1$ µL/min).

Although the integration of microelectrode arrays and neural cultures was not researched here, this project design will account for future integration requirements based on established parameters in the field and will serve as preparatory research for future projects.

Methodology

Computational Fluid Dynamics

Finite element analysis was performed on a simulated single microfluidic channel. The modular design allows single-channel flow analysis, saving computational resources and enabling extrapolation to the full device. The geometry was created as a CAD mockup in SolidWorks (Fig. 1).
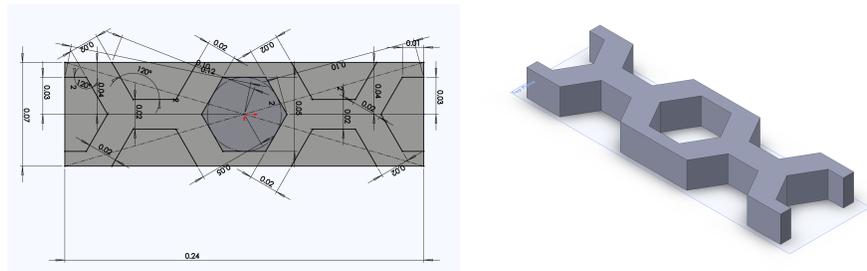
Figure 1. SolidWorks Channel Design. A: Sketch relations used to define the microfluidic channel dimensions. B: 3D representation of the single channel geometry with 0.2424mm height.

The completed geometry was imported into ANSYS Fluent (Fig. 2), where input and output faces were defined (highlighted in blue and green, respectively). Symmetry walls were defined on the left and right sides of the channel (highlighted in red).

The complete mesh structure (Fig. 3) was configured using double precision settings, with local sizing added specifically at the inlet and outlet faces to enhance precision (Fig. 4). These boundary regions were configured with a growth rate of 1.2 and a target mesh size of 0.25 μm. Surface mesh generation parameters were set with a minimum size of 0.2368038 μm and a maximum size of 1 μm. The geometry consisted solely of fluid regions with no void spaces, and fluid boundary types were set to wall conditions by default with no-slip conditions applied. Boundary conditions specified velocity inlet for the inlet face (0.0002 m/s, 0.0005 m/s, and 0.001 m/s) and pressure outlet for the outlet face. The two lateral channel walls were designated as symmetry boundaries to simulate the behavior of multiple parallel channels, with the entire region labeled as a fluid domain. Temperature effects were not considered in the simulation, with water modeled using its standard properties at room temperature.

A single boundary layer was implemented with default settings, comprising 6 layers, a transition ratio of 0.272, and a growth rate of 1.2 across all fluid regions and zones. Individual cell quality can be observed in the critical regions (Fig. 5), where the solver utilized polyhedral mesh elements with a growth rate of 1.2 and maximum cell length of
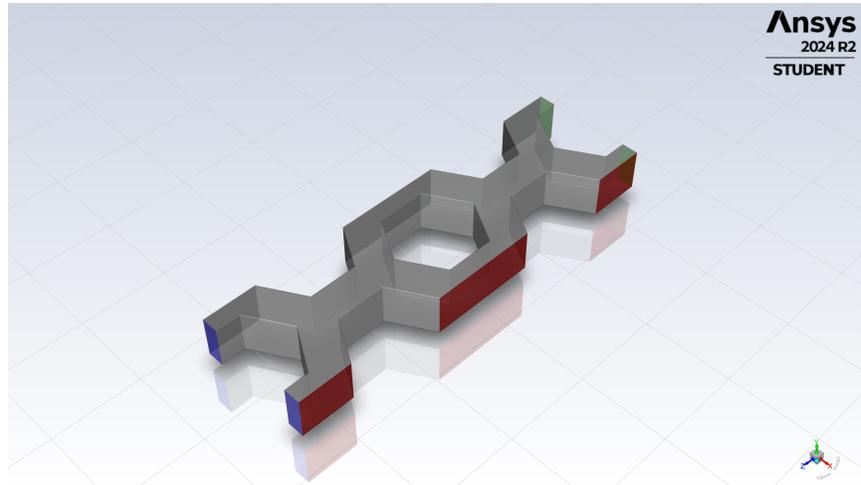
Figure 2. ANSYS Fluent Geometry Import. Imported channel geometry showing boundary condition definitions of the channel walls and inlet faces for fluid simulation.
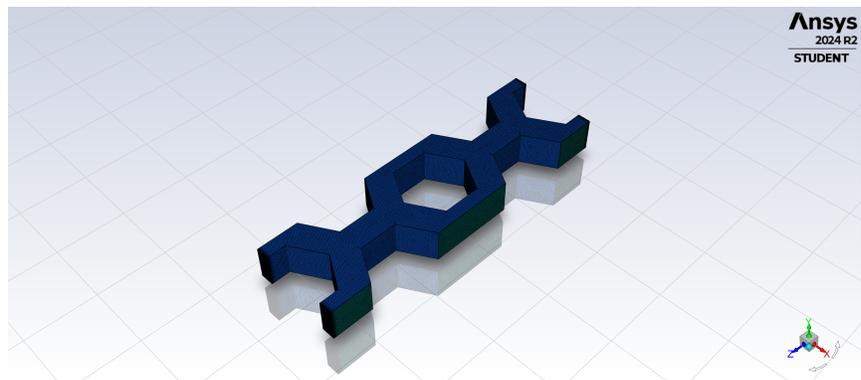
Figure 3. Complete Mesh Overview. Full mesh visualization of overall mesh quality across the channel geometry.
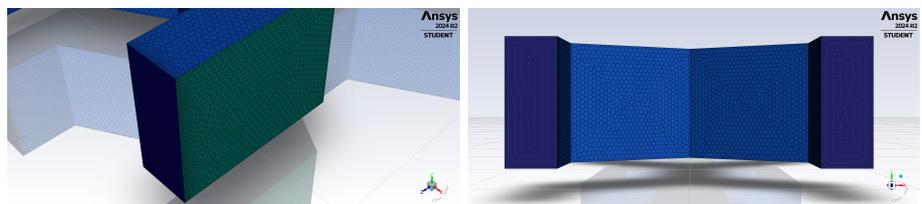
Figure 4. Detailed Mesh Views. A: Detailed view of mesh refinement at inlet region. B: Front view displaying mesh transition.

0.8 μm. Only laminar flow was modeled. The simulation used aluminum as the solid material and water as the fluid medium designated throughout the entire domain. The simulation was executed for 1000 iterations using the SIMPLEC solution scheme.

Fabrication

The microfluidic channel design was first designed in SolidWorks to establish the dimensions relationships of the device (Fig.1). This CAD design was then translated into a mask layout using LayoutEditor software. The final mask design consists of an
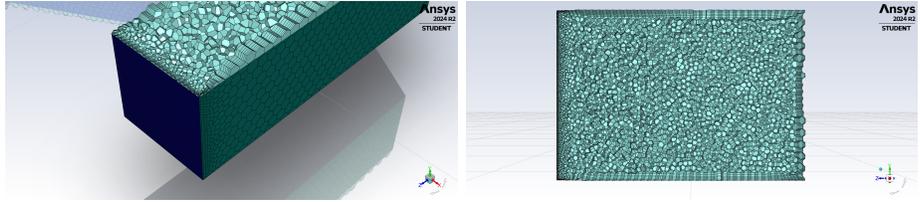
Figure 5. Individual Cell Visualization. A: Close-up view of polyhedral mesh elements near inlet region. B: Detailed visualization of individual cell quality in critical flow areas.

array of regular hexagonal wells with side lengths of 34.64 μm arranged in a honeycomb pattern (Fig.6). Microfluidic channels connecting each well were designed with widths of 20 μm. The complete layout was exported in GDSII format for direct-write lithography.
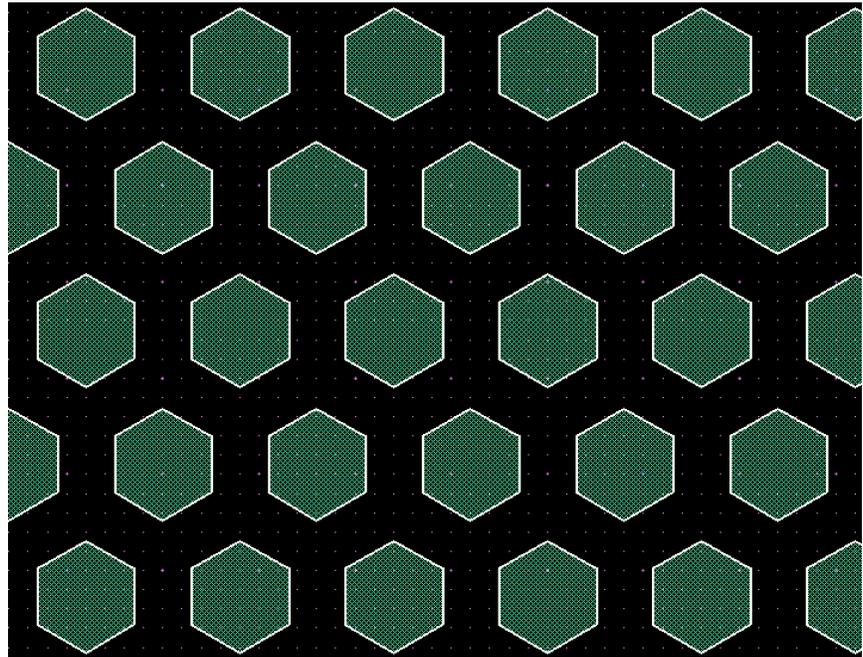
Figure 6. Photolithography Mask Layout. Final mask design showing the hexagonal well array pattern created in Layout Editor.

The microfluidic device was fabricated using standard photolithography techniques. A silicon wafer was cleaned with acetone, isopropyl alcohol, and deionized water before spin-coating with SU-8 1818 photoresist. The photoresist was spin-coated and soft-baked to remove excess solvent. The substrate was then exposed to UV light through direct-write lithography to define the microfluidic channel patterns. After exposure, a post-exposure bake, photoresist development, and a hard bake step was done to strengthen the patterned features. Final steps involved plasma ashing and a wet strip resist process to ensure cleaner feature definition. Finally, the device was sealed using a wafer bonding process to create the enclosed microfluidic channels, resulting in the final functional device. A detailed step-by-step fabrication process flow is shown in Fig. 7.

To measure the performance of the fabricated microfluidic device, a testing protocol was designed. The proposed protocol would connect the device's inlet and outlet ports to a pressure-driven flow system using UV-curable adhesive to create sealed connections, as shown in Fig. 8. The testing protocol will be done at specified flow rates ranging
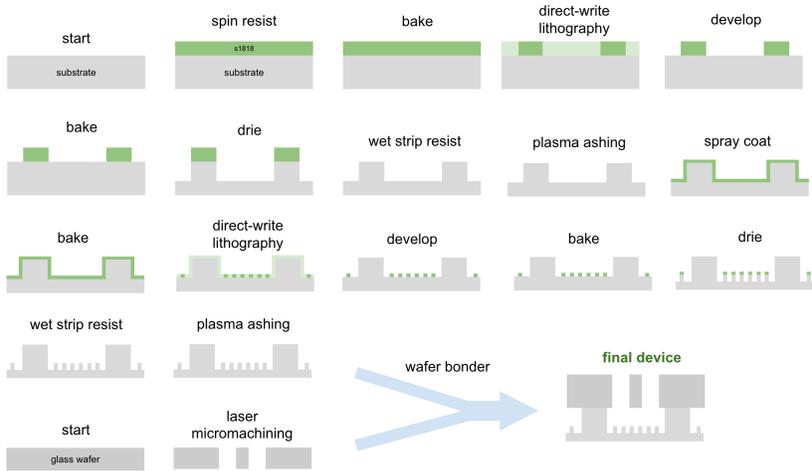
Figure 7. Microfluidic Device Fabrication Process Flow. Schematic illustration of the complete fabrication process to create the enclosed microfluidic device.

from $0.1 - 1$ µL/min. Pressure measurements would be recorded at both inlet and outlet ports to calculate the pressure drop across the device.
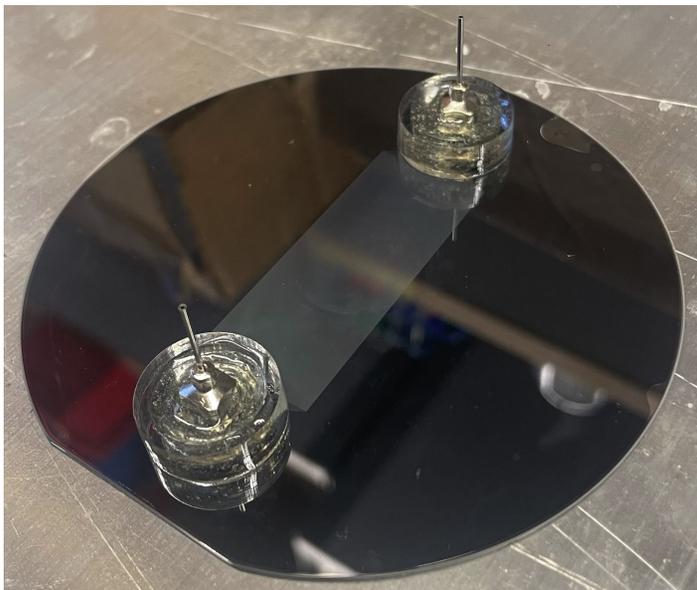
Figure 8. Microfluidic Device Testing Setup. The microfluidic device with two connecting ports for flow testing.

Results

Mesh Quality and Convergence Analysis

The final mesh optimization achieved 988,203 cells with over 3.8 million interior nodes, approaching the 1,000,000 computational limitations for ANSYS Student Edition while maintaining sufficient resolution for accurate flow field calculation. Mesh quality metrics confirmed the simulation reliability with an average orthogonal quality of 0.934

(minimum 0.317), average skewness of 0.008 (maximum 0.257), and maximum aspect ratio of 25.48. Residual convergence thresholds of 1×10^{-3} for continuity and 1×10^{-5} for velocity components were achieved.

The static pressure profile reveals two distinct pressure drop characteristics across the simulated channel segment. The average pressure decreases from approximately 850 Pa to 0 Pa, while maximum pressures peak at 1.58 kPa before dropping to 0 Pa at the outlet. At flow rates of 0.1–1 μL/min, pressure analysis revealed drops from 850 Pa to 0 Pa (average) and 1.58 kPa peak pressures across the simulated segment. Extrapolated to the full 50,000 μm device length, this indicates pressure differentials of 177 kPa (average) and 329 kPa (maximum). Photolithographic fabrication successfully produced the designed patterns, though with some edge roughness and corner rounding at feature interfaces. Future work will involve experimental flow characterization to validate computational predictions and optimize device performance.

The pressure drop across the full device length was extrapolated through an assumed linear relationship under the Hagen-Poiseuille equation:

$$\Delta P_{total} = \Delta P_{unit} \times \frac{L_{total}}{L_{unit}} \tag{1}$$

where ΔP_{unit} is the pressure drop across one unit, L_{unit} is the unit length, and L_{total} is the total device length.

For the average pressure drop:

$$\Delta P_{total} = 850 \, \text{Pa} \times \frac{50,000 \, \mu\text{m}}{240 \, \mu\text{m}} = 177,083 \, \text{Pa} \approx 177 \, \text{kPa} \tag{2}$$

For the maximum pressure drop:

$$\Delta P_{total} = 1,580 \, \text{Pa} \times \frac{50,000 \, \mu\text{m}}{240 \, \mu\text{m}} = 329,167 \, \text{Pa} \approx 329 \, \text{kPa} \tag{3}$$
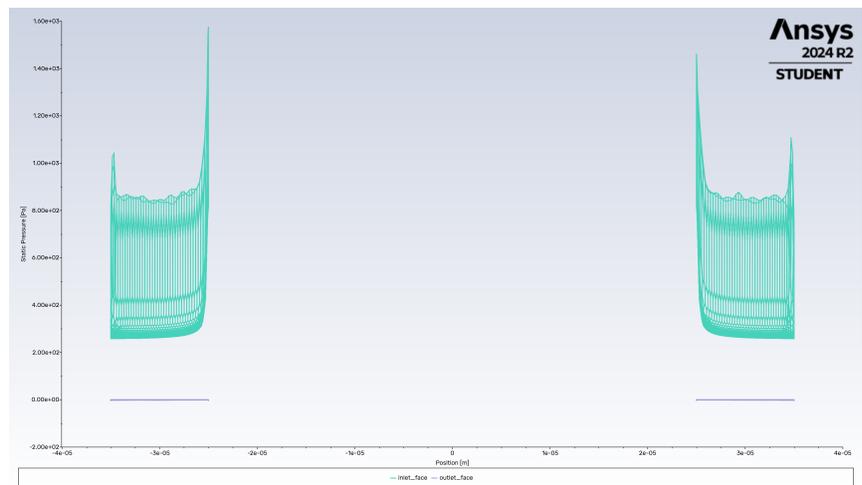
Figure 9. Static Pressure Distribution. Static pressure profile showing both average (850 Pa) and peak (1.58 kPa) pressure drops across the channel segment.

The static pressure distribution at the inlet face of the microfluidic channel reveals a notable gradient, with an average pressure of 3.08×10^2 Pa and localized peaks reaching 1.58×10^3 Pa at the corners as shown in Fig. 10. This pressure concentration at the corners is characteristic of fluid flow and arises due to abrupt changes in flow direction and velocity gradients. At the sharp corners, the fluid velocity decreases locally, leading

to a corresponding rise in static pressure as described by Bernoulli's principle. In 109
contrast, regions along the central inlet face experience more uniform flow, resulting in 110
lower average pressures. 111
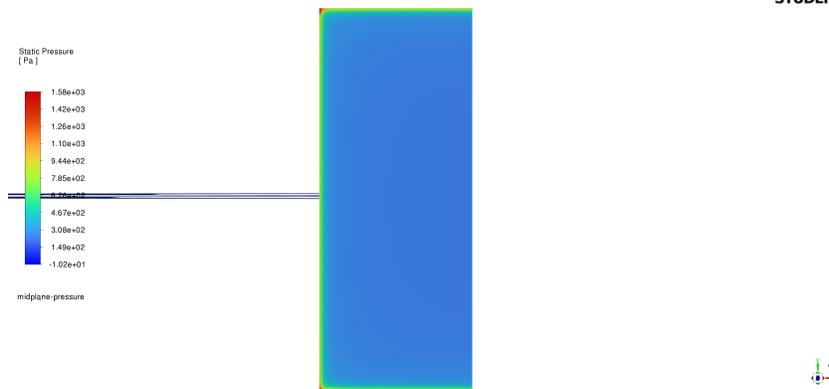
Figure 10. Static Pressure Distribution at Inlet. Static pressure profile for the inlet, with uniform pressure region and characteristic boundary gradients near the wall.

The static pressure distribution across the microfluidic channel exhibits a 112
characteristic gradient from inlet to outlet, as shown in Fig. 11 and detailed in Table 1. 113
The pressure measurements demonstrate a well-designed initial geometry that minimizes 114
pressure losses while maintaining stable flow conditions. 115
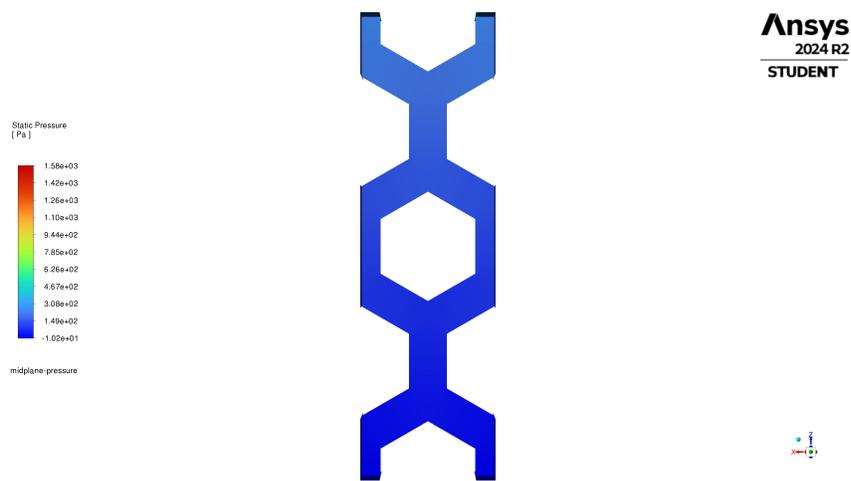
Figure 11. Static Pressure Distribution Across Channel. Static pressure profile illustrating the pressure drop across the length of a single microfluidic channel. The design's symmetry shows uniform flow distribution, with minimal pressure variations.

The velocity profile was found to be higher near the inlet and outlet channels and 116
symmetry walls (4.16×10^{-4} m/s) and lower in the main channel (4×10^{-5} m/s), as 117
shown in Fig. 12. 118

All quantitative measurements and analysis of the pressure distribution, including 119
inlet and outlet pressures, pressure gradients, and velocity measurements, are 120
summarized in Table 1 below. Additional results from simulating inlet velocity at 121
0.0005 m/s and 0.001 m/s are also included in the table. 122
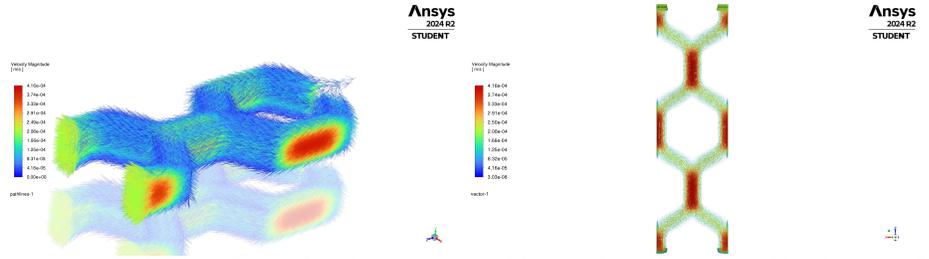
Figure 12. Velocity Distribution Across Channel. Velocity profile showing fluid flow pathlines (left) and top view (right) across the microfluidic channel. The pathlines illustrate the flow direction and velocity magnitude, with higher velocities (red) in the center and lower velocities (blue/green) near the walls.

The volumetric flow rate Q was calculated using the equation:

$$Q = A \times V \tag{4}$$

where A is the cross-sectional area of the inlet and V is the fluid velocity at the inlet. The inlet has dimensions of 0.025 mm × 0.04 mm, giving a cross-sectional area:

$$A = 0.025 \text{ mm} \times 0.04 \text{ mm} = 0.001 \text{ mm}^2 = 1 \times 10^{-9} \text{ m}^2 \tag{5}$$

For each inlet velocity, the volumetric flow rate was calculated as follows:
For $V = 0.0002$ m/s:

$$Q = (1 \times 10^{-9} \text{ m}^2)(0.0002 \text{ m/s}) = 2 \times 10^{-13} \text{ m}^3/\text{s} = 0.012 \text{ } \mu\text{L/min} \tag{6}$$

For $V = 0.0005$ m/s:

$$Q = (1 \times 10^{-9} \text{ m}^2)(0.0005 \text{ m/s}) = 5 \times 10^{-13} \text{ m}^3/\text{s} = 0.03 \text{ } \mu\text{L/min} \tag{7}$$

For $V = 0.001$ m/s:

$$Q = (1 \times 10^{-9} \text{ m}^2)(0.001 \text{ m/s}) = 1 \times 10^{-12} \text{ m}^3/\text{s} = 0.06 \text{ } \mu\text{L/min} \tag{8}$$

Table 1. Pressure Analysis of Microfluidic Units

Length (μm)	P_{in} (Pa)	P_{out} (Pa)	ΔP (Pa)	$\Delta P/L$ (Pa/μm)	Velocity$_{in}$ (m/s)	Flow Rate Q (μL/min)
240	≈ 850	0	850	3.54	0.0002	0.012
240	≈ 675	0	675	2.81	0.0005	0.03
240	≈ 1350	0	1350	5.63	0.001	0.06

Fabrication and Testing

The photolithographic fabrication process successfully produced the designed hexagonal well patterns. Two distinct pattern types were achieved: smooth-walled hexagonal wells and hexagons with gear-like teeth as shown in Fig. 13.

However, examination of the features under microscopy revealed deviations from the intended dimensions. Edge roughness and corner rounding were observed, particularly at the gear-tooth interfaces, possibly indicating that the fabrication resolution approached the limits of our photolithography process. While these imperfections are unlikely to impact the overall functionality of the device, they suggest that further optimization of exposure parameters and development conditions could improve pattern resolution.
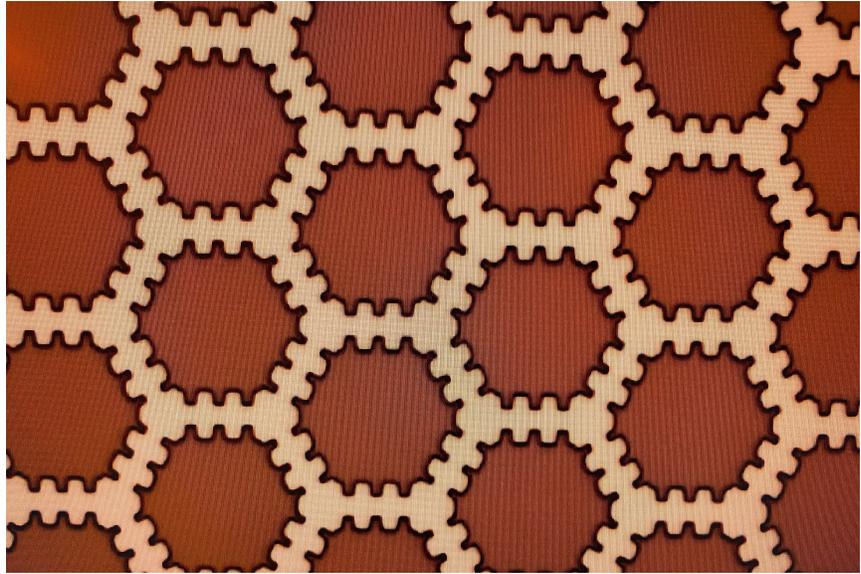
Figure 13. Microscopy of Fabricated Pattern. Optical microscope image showing the hexagonal-with-gear-teeth array pattern after fabrication.

While this testing setup was designed and the device was prepared for characterization, experimental flow measurements were not completed in this study. Future work will involve flow characterization and comparison with the computational fluid dynamics predictions to validate device performance.

Conclusion

This work demonstrated both computational modeling and fabrication capabilities for a future neuromorphic microfluidic platform. The computational fluid dynamics analysis achieved reliable convergence and revealed pressure and velocity distributions suitable for maintaining precise flow control. The fabrication process successfully produced hexagonal well arrays with two distinct patterns though with some edge roughness at feature boundaries, indicating areas for process optimization.

Future work would focus on: (1) experimental validation of computational predictions through flow characterization, (2) optimization of fabrication parameters to improve pattern fidelity at smaller scales, and (3) integration of the platform with neural network components. These steps will enable the development of a fully functional microfluidic system for future neuromorphic computing projects.

Acknowledgments

References

[1] Zhihao Xu et al. "Large-Scale Photonic Chiplet Taichi Empowers 160-TOPS/W Artificial General Intelligence". In: *Science (New York, N.Y.)* 384.6692 (Apr. 2024), pp. 202–209. ISSN: 1095-9203. DOI: 10.1126/science.adl1203.

[2] Rajeev Muralidhar, Renata Borovica-Gajic, and Rajkumar Buyya. "Energy Efficient Computing Systems: Architectures, Abstractions and Modeling to Techniques and Standards". In: *ACM Computing Surveys* 54.11s (Jan. 2022), pp. 1–37. ISSN: 0360-0300, 1557-7341. DOI: 10.1145/3511094. arXiv: 2007.09976 [cs]. (Visited on 12/14/2024).

[3] Pouya Houshmand, Jiacong Sun, and Marian Verhelst. "Benchmarking and Modeling of Analog and Digital SRAM In-Memory Computing Architectures". In: arXiv:2305.18335 (May 2023). DOI: 10.48550/arXiv.2305.18335. arXiv: 2305.18335 [cs]. (Visited on 12/14/2024).

[4] Lena Smirnova. "Biocomputing with Organoid Intelligence". In: *Nature Reviews Bioengineering* (May 2024), pp. 1–2. ISSN: 2731-6092. DOI: 10.1038/s44222-024-00200-6. (Visited on 06/02/2024).

[5] Moein Khajehnejad et al. "Biological Neurons Compete with Deep Reinforcement Learning in Sample Efficiency in a Simulated Gameworld". In: arXiv:2405.16946 (May 2024). arXiv: 2405.16946 [cs, q-bio]. (Visited on 06/02/2024).

[6] Hongwei Cai et al. "Brain Organoid Reservoir Computing for Artificial Intelligence". In: *Nature Electronics* 6.12 (Dec. 2023), pp. 1032–1039. ISSN: 2520-1131. DOI: 10.1038/s41928-023-01069-w. (Visited on 05/19/2024).

[7] Brett J. Kagan et al. "In Vitro Neurons Learn and Exhibit Sentience When Embodied in a Simulated Game-World". In: *Neuron* 110.23 (Dec. 2022), 3952–3969.e8. ISSN: 0896-6273. DOI: 10.1016/j.neuron.2022.09.001. (Visited on 07/08/2024).

[8] Spencer T. Seiler et al. "Modular Automated Microfluidic Cell Culture Platform Reduces Glycolytic Stress in Cerebral Cortex Organoids". In: *Scientific Reports* 12.1 (Nov. 2022), p. 20173. ISSN: 2045-2322. DOI: 10.1038/s41598-022-20096-9. (Visited on 05/19/2024).